MULTISCALE FINITE-VOLUME CVD-MPFA FORMULATIONS ON STRUCTURED AND UNSTRUCTURED GRIDS

ELLIOT PARRAMORE[†], MICHAEL G. EDWARDS[‡], MAYUR PAL[§], AND SADOK LAMINE[¶]

Abstract. This paper presents the development of finite-volume multiscale methods for quadrilateral and triangular unstructured grids. Families of Darcy-flux approximations have been developed for consistent approximation of the general tensor pressure equation arising from Darcy's law together with mass conservation. The schemes are control-volume distributed (CVD) with flow variables and rock properties sharing the same control-volume location and are comprised of a multipoint flux family formulation (CVD-MPFA). The schemes are used to develop a CVD-MPFA based multiscale finite-volume (MSFV) formulation applicable to both structured and unstructured grids in two-dimensions. The basis functions are a key component of the MSFV method, and are a set of local solutions, usually defined subject to Dirichlet boundary conditions. A generalisation of the Cartesian grid Dirichlet basis functions described in [20] is presented here for unstructured grids. Whilst the transition from a Cartesian grid to an unstructured grid is largely successful, use of Dirichlet basis functions can still lead to pressure fields that exhibit spurious oscillations in areas of strong heterogeneity. New basis functions are proposed in an attempt to improve the pressure field solutions where Neumann boundary conditions are imposed almost every where, except corners which remain specified by Dirichlet values.

Key words. Multiscale Finite Volume Method & MSFV & Control-volume Distributed Multipoint Flux Approximation & CVD & MPFA

AMS subject classifications.

1. Introduction. Subsurface reservoirs generally have complex geological and geometrical features, such as faults fractures, pinchouts, shales and layers defined on varying length scales. In addition the effect of heterogeneity leads to further multiscale features that cannot be modelled with desired precision on relatively coarse meshes. This has led to development of a variety of multiscale methods, both non-iterative and iterative with analysis, on structured and unstructured grids and applications including fractures over the last decade e.g. [17, 20, 21, 10, 3, 16, 19, 22, 27, 14, 1, 26, 30], and with the exception of [28, 29], all other unstructured grid MSFV formulations that we are aware of are based on a 2-point flux. In this work we present the generalisation of the Cartesian MSFV method first presented in [20] to unstructured grids in two dimensions using the CVD-MPFA formulation. The formulation is non-iterative. The basis functions and finescale solutions are computed using a CVD-MPFA formulation which is consistent on structured and unstructured grids without any K-orthogonality requirement. Two types of basis function are considered; the first results from using Dirichlet boundary conditions and the resulting MSFV method reduces to precisely that of [20] when on a Cartesian grid, the second results from employing essentially

[†]Zienkiewicz Centre for Computational Engineering (ZCCE)
Swansea University, *Singleton Park, Swansea, SA2 8PP, UK*
436277@swansea.ac.uk

[‡]Zienkiewicz Centre for Computational Engineering (ZCCE)
Swansea University, *Singleton Park, Swansea SA2 8PP, UK*

[§]Maersk Oil, *Copenhagen, Denmark*

[¶]Shell, *Kessler Park 1, 2288 GS Rijswijk Zh, The Netherlands*

Neumann boundary conditions (except at corners) leading to a new type of basis function, and MSFV variant. The unstructured MSFV framework and new basis functions were first proposed in [28, 29] and proved to be beneficial in extending the MSFV method to unstructured grids. This paper contains a substantial revision of [28, 29] together with significant further work.

In recent years several discretisation methods that can treat unstructured grids together with discontinuous and anisotropic permeability fields have been developed. These schemes include the finite volume schemes, e.g., [2, 9, 8, 24, 23, 11, 31, 12, 13] and references therein, while other methods e.g. [4, 7, 6, 18, 5, 15, 25] (and references therein) offer an alternative these methods involve more degrees of freedom. In this paper we employ cell centred families of continuous Darcy-flux approximations that have been developed for consistent approximation of the general tensor pressure equation arising from Darcy's law together with mass conservation [9, 13]. In particular the symmetric positive definite scheme of [13] is the main scheme used here for unstructured grids. These finite-volume schemes are control-volume distributed (CVD) with pressure and rock properties sharing the same location in a given control-volume and are comprised of a multipoint flux family formulation (CVD-MPFA), employing a single degree of freedom per control-volume. These schemes are used to develop CVD-MPFA based multiscale finite-volume formulations, applicable to both structured and unstructured grids in two-dimensions. An example using MSFV with a two-point flux approximation versus MSFV with CVD-MPFA on a non K-orthogonal grid is presented, the results motivate the need for the development of MSFV based on the CVD-MPFA formulation presented below.

Performance of the CVD-MPFA based multiscale formulations is presented for a range of grid types on both structured and unstructured grids. The methods are applied to domains with homogeneous and heterogeneous permeability fields involving a range of test cases.

The choice of basis functions is found to be crucial in the multiscale finite-volume formulation. Boundary condition constraints and consequences of basis function formulation, together with implications of scheme and grid type are presented. The development of a CVD-MPFA based multiscale formulation leads to a novel approach for fine scale modeling on unstructured grids. The results presented include pressure fields, and transport of tracer concentration for heterogeneous examples, and demonstrate the benefits of the new formulation.

After a brief review of the flux continuous finite volume schemes employed, the new multiscale formulation is presented, followed by results and conclusions.

2. Pressure Equation Formulation. Here we focus on the discretization of the elliptic partial differential equation for pressure encountered in reservoir simulation arising from Darcy's law and mass conservation for single phase flow. This is also representative of the form of the pressure equation for multi-phase flow. We now consider the elliptic pressure equation

$$-\nabla \cdot (\mathbf{K}\nabla\phi) = 0, \tag{2.1}$$

on a domain Ω where ϕ is the pressure and $\mathbf{K}$ is an elliptic permeability tensor (divided by a constant viscosity) that can be spatially varying and heterogeneous. The Darcy velocity is given by $\mathbf{v} = -\mathbf{K}\nabla\phi$. Eq.2.1 is solved here subject to Neumann

and/or Dirichlet conditions, specified typically on exterior or interior boundaries ($\delta\Omega$). Pressure is specified at least at one point in the domain Ω or on the domain boundary $\delta\Omega$ and similarly for subdomains (when multiscale) to ensure that the problem is well posed.

3. Flux-continuous Approximation. Finite volume schemes are derived by first integrating each flow equation over a control-volume and then introduce an approximation of the normal control-volume face flux, which ensures that local conservation is guaranteed. The control-volume definition depends on the fundamental choice between being cell-vertex and cell-centred. Here we use a cell-centred approximation. The cell-centred control-volume is defined by the primal grid cell, details of the discretizations are outlined below, we refer to [9, 13] for full details. The primal grids considered in this paper are comprised of triangular and quadrilateral meshes. Eq.2.1 is integrated over each cell-centred control-volume $i = 1, ..., N_E$, to yield

$$-\oint_{\delta\Omega_i} (\mathbf{K}\nabla\phi) \cdot \vec{n} dS = 0, \tag{3.1}$$

by the Gauss Divergence theorem, where $\delta\Omega_i$ denotes the boundary of the i^{th} grid cell (control-volume) Ω_i and $\hat{\vec{n}}$ is the outward normal vector with respect to the boundary $\delta\Omega_i$ and dS is a boundary face increment. The discrete boundary integral is performed over the boundary segments of $\delta\Omega_i$. A discrete normal flux approximation is formed with respect to the faces of each grid cell. The fluxes are expressed in terms of a local approximation of the general tensor $\mathbf{T}$ operating on local discrete pressure differences such that normal flux continuity is preserved as discussed below.

3.1. Cell Centred, Control-volume Distributed (CVD). In a cell-centred formulation the primal grid cells act as control-volumes over which the Gauss divergence theorem is applied and approximated. Following [13], each grid cell is assigned a grid point (nodal point) $\mathbf{x_i}$, usually equal to the cell centre. Flow variables and rock properties are distributed (assigned) to the grid cells and are therefore control-volume distributed (CVD). The value of the numerical solution in the cell is denoted by $\Phi_i = \phi(\mathbf{x_i})$. Two adjacent grid cells are termed neighbours if they share the same cell interface or cell edge. The permeability (conductivity) tensor $\mathbf{K}$ is assumed to be piecewise constant, with respect to cell values (see Fig 1(a)).

3.1.1. Cluster and Dual-Cell. A *cluster* c_j is defined by the N_f^j cells attached to a common grid vertex j. A *dual-cell* is defined as follows: For each cell edge k attached to the vertex of the *cluster*, connect the edge mid-point m_k to the grid cell centres of the two neighbouring cells within the cluster that share the common edge. The *dual-cell* is defined by the resulting polygon comprised of the contour segments connecting the N_f^j cell mid-points as indicated by the shaded red area in Fig 1(b). An analogous definition of the dual cell is used in the multiscale finite volume method.

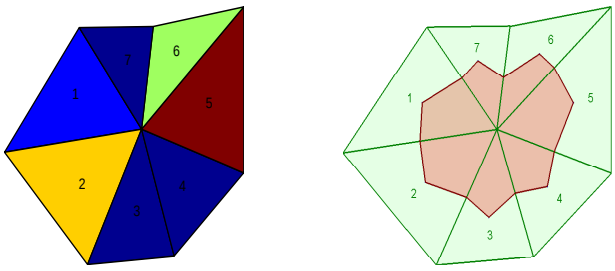

(a) (b)

FIG. 1. *(a) Illustartion of piecewise continuous permeability across each cell (b) Corresponding dual cell (shaded red) for the cluster*

$Sub-Cell$ and $Sub-interface$. Subcells result when the dual-cells overlay the primal triangular or quadrilateral grid. Each primal quadrilateral is then comprised of four quadrilateral *sub-cells* and each triangle is comprised of three quadrilateral *sub-cells*, again note Fig.1(b) where each primal cell has a quadrilateral subcell for every cluster they are attached to. The edge midpoint m_k divides a cell interface into two segments or *sub-interfaces*.

3.2. Flux and Pressure Continuity Conditions. One of the main advantages of the CVD-MPFA formulation is that it involves a single degree of freedom per control-volume, in this case the primal grid cell pressure Φ_i, while maintaining continuity in pressure and normal flux across the control-volume faces. This is achieved by introducing local auxiliary interface pressures on control-volume faces that are expressed in terms of the global pressure field via local algebraic flux continuity conditions, which are imposed across the control-volume faces, prior to matrix assembly and solution process. This leads to the generalisation of the classical 2-point flux approximation with transmissibility coefficient proportional to the harmonic mean of adjacent permeabilities, [**?**], and again we refer to [13] for more details.

Local Interface Pressures
Here point-wise pressure continuity is imposed by introducing an auxiliary interface pressure on each control-volume *sub-interface*. For the cell centred formulation the continuity point is placed on the *sub-interface* between the primal cell edge mid-point and edge vertex, yielding N_f^j interface pressures per j^{th} dual-cell. The quadrature point is parameterized by the variable q where $0 < q \leq 1$, and leads to a family of schemes, $q = 1$ being the default quadrature at the triangle edge midpoint.

3.2.1. Triangle Pressure Support TPS. In these schemes the pressure assumes a local piecewise linear variation over each resulting pressure sub-triangle defined inside a subcell. The cell-centred pressure sub-triangle is defined by joining the primal triangle cell centre, interface pressure point on the primal triangle right-edge, interface pressure point on the primal triangle left-edge and back to the primal triangle centre, leading to triangle pressure support (TPS) Fig.2. Triangle pressure support (TPS) is defined over the sub-triangle by the three pressure points $\Phi_i, \Phi_1^f, \Phi_2^f$

and the local TPS pressure approximation is defined by

$$\phi = (1 - \xi_1 - \xi_2)\Phi_i + \xi_1\Phi_1^f + \xi_2\Phi_2^f. \tag{3.2}$$

where Φ_1^f, Φ_2^f are local interface pressures and Φ_i is the cell-centred primal pressure for cell i. The position vector shares an analogous approximation over each sub-triangle with ϕ replaced by $\mathbf{r}$ in Eq.3.2. The quadrature point $q = 2/3$ indicated in Fig.2, yields the optimal symmetric positive definite scheme [13], and has been used here.

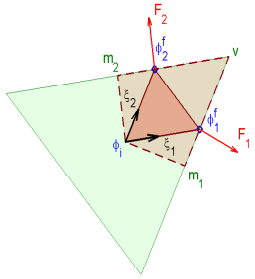

FIG. 2. *Triangle Pressure Support (TPS): illustrated quadrature q = 2/3 for a cell centred formulation*

3.2.2. Local Algebraic Flux Continuity. The discrete subcell Darcy velocity is obtained by substitution of the sub-triangle approximation of Eq.3.2 and analogous position vector approximation into the velocity vector

$$v_h = \begin{pmatrix} u \\ v \end{pmatrix} = -\mathbf{K} \begin{pmatrix} y_{\xi_2} & -y_{\xi_1} \\ -x_{\xi_2} & x_{\xi_1} \end{pmatrix} \frac{1}{\mid J \mid} \begin{pmatrix} \phi_{\xi_1} \\ \phi_{\xi_2} \end{pmatrix} \tag{3.3}$$

where $\mid J \mid$ is the local discrete Jacobian. Resolution of the discrete velocity onto the sub-interface outward normal vector $\vec{n}_1 = ((y_v - y_{m_1}), -(x_v - x_{m_1}))$ leads to a flux approximation

$$F^1_{v,m_1} = v_h \cdot \vec{n}_1 = -(T^1_{11}\phi_{\xi_1} + T^1_{12}\phi_{\xi_2})|^1_{v,m_1} \tag{3.4}$$

where it is understood that the coefficients T^1_{11}, T^1_{12} result from local discrete flux resolution, and are local subcell approximations of the general elliptic tensor coefficients $\mathbf{T}$ defined via the Piola transform (see e.g. [4]) where $\mathbf{T} =\mid J \mid \mathbf{J}^{-1}\mathbf{K}\mathbf{J}^{-T}$, and $\phi_{\xi_j} = (\Phi_j^f - \Phi_i), j = 1, 2$ are the resulting potential differences between the interface pressures and cell-centred pressures [13].

Therefore the two resulting discrete normal *sub-interface* flux components per subcell are expressed as

$$F_i = -(T_{i,1}\phi_{\xi_1} + T_{i,2}\phi_{\xi_2})|_{i=1,2} \tag{3.5}$$

where $i = 1, 2$ are the local flux indices. Eq.3.5 is the subcell view of the fluxes. This formulation applies to arbitrary polygonal grids resulting from any combination of quadrilateral and or triangular grids.

Continuity of discrete pressure and normal flux across each *sub-interface* is satisfied locally within each dual-cell by construction. The respective N_f^j interface pressures

per j^{th} dual-cell and corresponding cell centred pressures located on the dual-cell perimeter are used to define $2N_f^j$ subcell fluxes c.f. Eq.3.5 per subcell, which are used in turn to form N_f^j normal flux continuity conditions over the N_f^j sub-interfaces. The flux continuity conditions are written as

$$F_i = -(T_{11}\phi_\xi + T_{12}\phi_\eta)|^i = (T_{21}\phi_\xi + T_{22}\phi_\eta)|^{i+1}, \quad i = 1, ..., N_f^j \tag{3.6}$$

where the superfixes i and $i+1$ indicate the respective left and right hand subcells either side of sub-interface i for $i = 1, ..., N_f^j$, with respect to an anticlockwise view of the cluster 3.6 then when $i = N_f$, $i+1$ is set to unity, closing the loop.

The N_f^j sub-interface pressures are expressed in terms of the cell-centred pressures via the corresponding N_f^j normal flux continuity conditions of Eq. 3.6 and are thus locally eliminated from the system in each cluster prior to the global pressure solve [13].

3.3. Flux Approximation. The discrete flux F across a cell sub-interface is (after application of the continuity conditions) written as a linear combination of grid cell centre values Φ_i associated with the dual cell:

$$F = -\sum_{i \in N_F^j} t_i \Phi_i, \tag{3.7}$$

where N_F^j is the set of grid points involved in the flux approximation. All consistent discretizations satisfy the condition $\sum_{i \in N_F^j} t_i = 0$ [13]. The net cell centred flux across each cell-interface (triangle-edge) is comprised of two sub-interface fluxes, calculated by assembly. The zero divergence approximation of Eq.3.1 over each primal cell is achieved by local assembly of sub-interface fluxes, yielding a global $N \times N$ matrix, acting on the primary pressure vector of length N (number of primal grid cells).

4. Multiscale Formulation. The multiscale formulation employs a coarse grid and a fine grid and is a two grid level formulation. The coarse grid is comprised of a number of coarse cells that may be structured or unstructured. A coarse dual grid is then defined from the primal coarse grid, where each coarse dual-cell is defined relative to a primal coarse grid vertex. The coarse dual-cells are each comprised of a contour that joins coarse cell centres that surround a common primal coarse grid vertex, where the contour connects adjacent coarse cell centres via the common coarse cell-edge midpoints, Fig.1(b).The fine grid is defined via a specified refinement of the coarse cells. The coarse cell refinement is constrained to conform to the resulting boundary segments of the respective contours in each coarse cell. The presence of two grids is exploited by the use of both fine-scale and coarse-scale operators in the multiscale method. The fine scale operator results from the approximation of Eq.3.1 using the above outlined TPS formulation, denoted here now by

$$L_h \phi_h = 0 \tag{4.1}$$

where ϕ_h is the fine scale solution. The coarse scale operator is derived as an approximation of Eq.3.1 on a coarse grid, via a basis function formalism described in sec.4.1

below and denoted

$$L_H \phi_H = 0 \tag{4.2}$$

where ϕ_H is the coarse scale solution. The multiscale procedure can be described by three main steps;

1. Basis functions are defined over each coarse dual cell by a set of local fine scale solutions, computed according to a prescribed set of independent boundary conditions per dual cell. One basis function is defined for each coarse cell centred node belonging to a dual cell. The basis functions provide the link between coarse and fine grids, and are used to determine a coarse grid operator.

2. A coarse grid solution of the reservoir problem is then computed on the coarse grid using the coarse operator.

3. The coarse grid solution is then used to define Neumann boundary conditions with normal flux prescribed on the boundaries of each coarse cell ensuring flux is continuous between neighbouring coarse cell boundaries. A fine scale pressure and flux field is then computed over each coarse cell, subject to the Neumann flux conditions resulting from the coarse grid solution, with pressure specified at each coarse cell centre.

The original MSFV formulation has been developed for Cartesian grids and follows [20, 16]. We introduce an unstructured grid generalisation of the Cartesian Dirichlet boundary conditions presented in [16]. This boundary condition treatment requires that grid cells overlay the coarse dual-cell boundaries such that boundary nodes become cell centres. Special boundary meshing is introduced to achieve this, and is discussed further below with reference to Fig's. 3, 6. The advantage here is that boundary conforming Dirichlet boundary conditions are imposed without requiring special boundary discretization or ghost points, and the unstructured method generalises naturally for multiscale approximation. We refer to the resulting basis functions as embedded Dirichlet conditions.

4.1. Basis Functions. A cell-centred formulation is considered here. After definition of a coarse grid, the coarse cells are refined so as to preserve the boundary contour of the dual cell, as illustrated by the dark shaded region in Fig. 3(a,b), where conventional dual-cell boundary conforming grids are shown. Thus dual grid cells are defined with respect to the (coarse grid) cluster vertices.

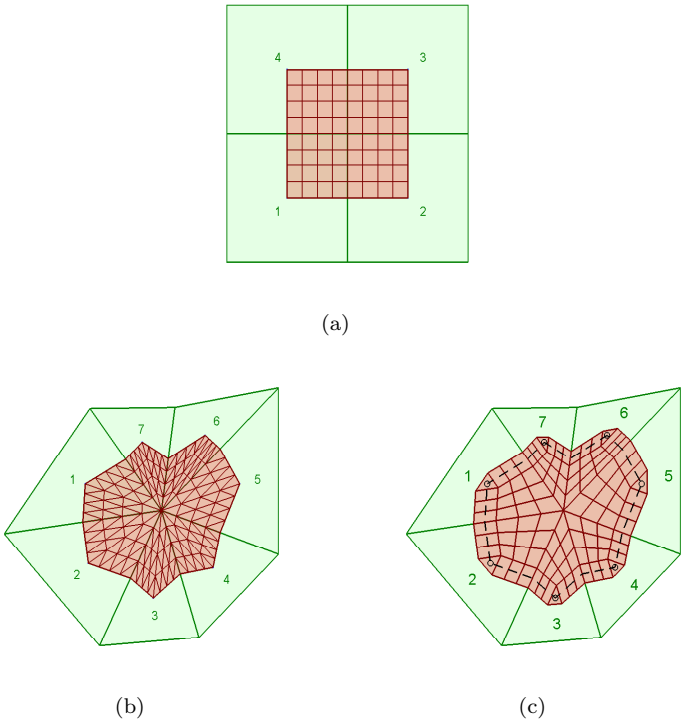

(a)

(b) (c)

FIG. 3. *Coarse grid cluster with dual-cell boundary conforming fine scale grid (a) Cartesian grid (b) Unstructured grid (c) Unstructured grid with embedded coarse dual-cell boundary*

Standard MSFV basis functions are derived following the Multiscale Finite Element (MSFE) basis functions proposed by [17] and are used to determine effective transmissibilities for the coarse grid operator and for fine grid boundary operators. Fine grid boundary (flux) conditions are defined on the boundaries of each coarse dual cell from the coarse grid solution, using transmissibilities that are consistent with the coarse grid operator and lead to local conservation between neighbouring dual cells. For every coarse dual cell, there are N_f^j basis functions, one for each coarse cell center node belonging to the coarse dual cell. The basis function boundary conditions for the standard MSFV method are identical to those used in MSFE basis functions where either a bilinear interpolation is used to define dirichlet boundary data, or a 'reduced boundary condition' is used to define the boundary dirichlet data [17, 20, 16]. The reduced boundary condition is obtained by solving a reduced elliptic problem along each edge of the coarse dual boundary. Currently MSFV basis functions have been defined over Cartesian grids where the dual grid is also uniform [20, 16]. The primary focus of this work is on the development of MSFV on quadrilateral and triangular unstructured grids together with appropriate basis functions.

For the purpose of this paper, the basis functions proposed in previous MSFV work are referred to as "Dirichlet basis functions" and are described in the next section, 4.1.1, along with the embedded generalisation to unstructured grids. A new type of basis function is introduced in Section 4.1.2 and referred to as "Neumann-D basis functions". Neumann-D basis function boundary conditions are simpler to implement, and yield stable results on any grid type and for highly heterogeneous permeability

fields.

4.1.1. Embedded Dirichlet Basis Functions. The Dirichlet basis functions, denoted ϕ^D, are essentially bilinear for each homogeneous quadrilateral dual cell over a regular domain Fig.5(a). Generalised Dirichlet basis functions involve specifying ϕ^D on the boundary of each coarse dual cell. A Dirichlet basis function is defined for each coarse cell-centered node belonging to a cluster. For the i^{th} basis function $\phi_i^D(\mathbf{x})$ (where $\mathbf{x}$ is the position vector), at the i^{th} coarse cell-centred node (corner) of the dual cell $\phi_i^D(\mathbf{x_i}) = \mathbf{1}$ and at all other cell centre nodes j of the dual cell $\phi_i^D(\mathbf{x_j}) = \mathbf{0}$ for $j \neq i$, with linear interpolation defining specified Dirichlet data on the fine cell edges that lie on the coarse dual cell grid boundary between all adjacent corners, Fig.5(b).

There are two aspects to be addressed in the generalisation of Dirichlet basis functions to cell-centred duals on unstructured grids.

1) Since the boundary of an unstructured dual is not a straight line between cell centers, Fig.1b, interpolating the dirichlet data along the dual-cell boundary can be achieved in several ways. The method used here involves interpolation over the entire arc length, that is the combined edge length of the boundary between two coarse centers, (corners of the dual). The arc length is mapped to a straight line of length equal to the arc length, Fig.4, which is used to define the interpolation of dirichlet data. This allows any grid geometry to be used.

2) For a cell centred method, imposition of Dirichlet boundary conditions is usually achieved, either via the use of ghost cells, or by defining values at cell edge mid-points (for those cell-edges laying on the boundary). Ghost points do not generalise naturally on unstructured grid dual-cell boundaries as they are not boundary conforming, while edge based Dirichlet boundary conditions require a special discretization at boundaries [28, 29]. In order to address the boundary alignment issue, a different method of meshing is used, motivated by that used in [16] for Cartesian grids, but now generalised to any dual-cell boundary geometry that may result from an unstructured grid. In contrast to the boundary aligned meshing initially described, Fig.3, the fine scale grid is generated such that the boundary of each coarse dual-cell is 'straddled' or overlaid by the finescale primal grid Fig.6a, such that boundary nodes correspond to the cell centres of the overlaying boundary cells. In an unstructured grid this requires hybrid meshing, where both triangular and quadrilateral finescale cells are used such that the coarse scale dual-cell boundary is embedded in the set of finescale dual mesh perimeter cells. This also places a further constraint on the finescale meshing of each coarse cell. The Dirichlet basis function boundary conditions however, are much easier to implement as they can now be set directly on boundary cell centres rather than faces Fig.6b. An example fine grid with embedded finescale dual mesh perimeter cells is shown in Fig.11. This unstructured boundary condition treatment generalises naturally for multiscale approximation. We refer to the resulting basis functions as embedded Dirichlet conditions.

Eq. 4.1 is then solved on the fine scale grid, defined over the coarse dual cell, subject to the embedded Dirichlet boundary conditions, using the cell-centred CVD-MPFA method. Thus the pressure and flux field for the i^{th} basis function is calculated. The process is repeated for each basis function corresponding to each corner node of the dual cell. The resulting solutions define the embedded Dirichlet basis functions, an

example is shown in Fig.6c,

The resulting basis function solutions yield coefficients that satisfy the consistency condition $\sum_{i \in N_F^j} t_i = 0$ for local coarse and fine transmissibilities, (discussed further in the flux consistency section below) and lead to stable reconstructed finescale pressure fields in most cases c.f. (Section 5).

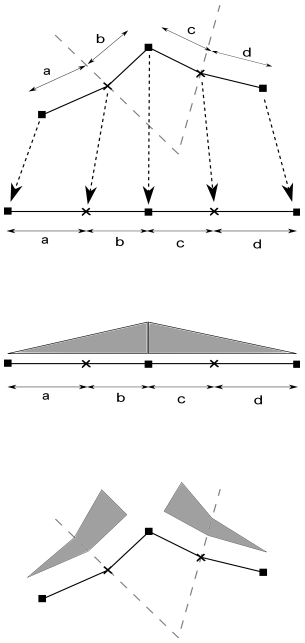

FIG. 4. *Dirichlet interpolation along an unstructured coarse dual edge. From top to bottom: Coarse dual edge (arc length) is mapped to a straight line, dirichlet data is interpolated between* 0 *and* 1*, interpolated data is mapped back to arc length.*

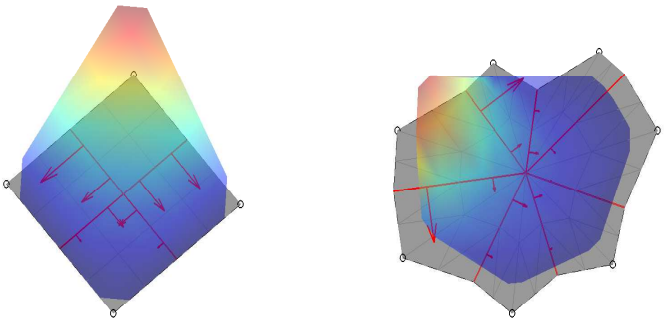

(a) (b)

FIG. 5. *Embedded Dirichlet basis function example across a dual cell: (a) Cartesian grid (b) Delaunay grid*

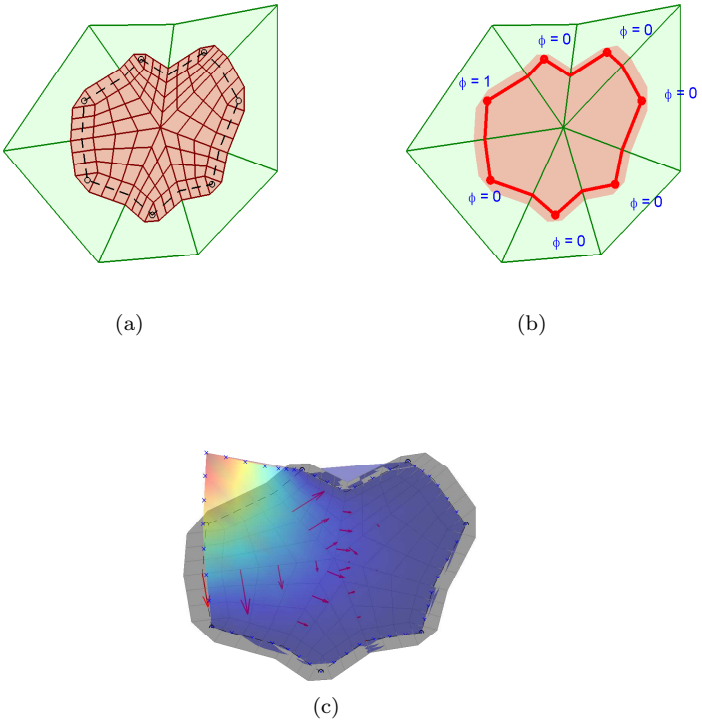

(a) (b)

(c)

FIG. 6. *Alternative 'embedded' fine scale meshing : (a) unstructured grid with embedded coarse dual-cell boundary (b) Embedded Dirichlet Boundary condition implementation (c) Example basis function pressure field*

4.1.2. Neumann-D Basis Functions. Neumann-Dirichlet basis functions ϕ^{N_D} are now defined over the coarse dual-cells. Away from coarse cell centre nodes Neumann-Dirichlet basis functions involve the specification of zero flux on dual cell boundaries, which basically replaces the (Dirichlet condition) basis function boundary data interpolant specification *almost everywhere*, except at the corners of the dual defined by the cell centres, where ϕ^{N_D} remains specified by pointwise Dirichlet data. We shall refer to these basis functions as *Neumann-D* basis functions, to reflect the primarily Neumann nature of these basis functions together with (coarse cell-centre) point-wise Dirichlet conditions, and denote the basis functions by ϕ^{N_D}. A Neumann-D basis function is defined for each cell-centered node belonging to a cluster.

For the i^{th} basis function $\phi_i^{N_D}(\mathbf{x})$, belonging to the i^{th} coarse cell-centred node (corner) of the dual cell $\phi_i^{N_D}(\mathbf{x_i}) = \mathbf{1}$ is set in the associated fine grid corner cell centre, and for all other coarse cell-centred nodes j, of the dual-cell $\phi_i^{N_D}(\mathbf{x_j}) = \mathbf{0}$ in the respective associated fine grid corner cell centres for $j \neq i$, while zero normal flux is imposed over the rest of the boundary of the dual cell apart from the specified cell-centre values, Fig. 7a. Eq. 4.1 is then solved on the fine scale grid, defined over the dual-cell, using the above cell-centred method. Thus we solve

$$-\nabla \cdot (\mathbf{K}\nabla\phi^{N_D}) = 0. \tag{4.3}$$

over each dual-cell Ω_D subject to $-\mathbf{K}\nabla\phi^{N_D}\mathbf{.\hat{n}} = \mathbf{0}$ on boundary $\partial\Omega_D \backslash \{\mathbf{x_1}, \mathbf{x_2}, ...\mathbf{x_{N_f}}\}$ where $\mathbf{x_1}, \mathbf{x_2}, ...\mathbf{x_{N_f}}$ are the N_f associated fine cell centres of the corner nodes belong-

ing to the dual-cell, and for the i^{th} basis function corresponding to the i^{th} coarse cell centre node $\phi_i^{N_D}(\mathbf{x_i}) = \mathbf{1}$ while $\phi_i^{N_D}(\mathbf{x_j}) = \mathbf{0}$ for $j \neq i$. The definition is repeated for all coarse cell-centre corner nodes of each dual-cell and the solutions define the Neumann-D basis functions.

4.2. Fine Scale Operator.
Once basis function solutions are determined the procedure for defining the local transmissibility matrix is the same for either basis function type and is an unstructured generalisation of the procedure for the standard MSFV method [20, 16]. For each basis function solution a set of fine scale fluxes is computed over each of the coarse scale sub-interfaces and denoted by f_i^* with respect to the i^{th} coarse sub- interface in the coarse dual cell. The number of components of the vector of fine scale fluxes f_i^* is equal to the number of fine cells on a coarse cell subinterface inside a dual cell. The vector of fine scale fluxes on the i^{th} coarse subinterface is expressed in terms of the coarse dual cell-centred pressures as

$$f_i^* = \Sigma_{j=1}^{N_f} t_{i,j}^* \phi_{H_j} \tag{4.4}$$

where $t_{i,j}^*$ is the corresponding vector of transmissibilities, summation is over the coarse cell nodes of the dual cell. The $t_{i,j}^*$ are then determined from Eq.4.4 via the basis functions, and setting $\phi_{H_i} = 1$ and $\phi_{H_j} = 0$ for $j \neq i$ when using Neumann-D basis functions, with f_i^* computed via the CVD-MPFA operator acting on the corresponding known i^{th} basis function (fine grid) solution, (replace $\phi_i^{N_D}$ by ϕ_i^D for embedded Dirichlet basis functions). Starting with coarse sub-interface 1, the $t_{1,j}^*$ are determined via the local flux vector calculated on the interface for each basis function $j = 1, ...N_f$. The process is repeated for each interface $i = 1, ...N_f$ which determines the flux coefficients for the N_f faces, and gives rise to the transmissibility matrix of fine scale coefficients

$$\mathbf{T}^* = \begin{bmatrix} t_{1,1}^* & t_{1,2}^* & \cdots & t_{1,n}^* \\ t_{2,1}^* & t_{2,2}^* & \cdots & t_{2,n}^* \\ \vdots & \vdots & \ddots & \vdots \\ t_{n,1}^* & t_{n,2}^* & \cdots & t_{n,n}^* \end{bmatrix} \tag{4.5}$$

such that every component '$t_{i,j}^*$' of Eq.4.5 is a vector of flux values corresponding to the sub interface i as influenced by the cell centre j.

4.3. Flux Consistency: Necessary Condition. The flux consistency condition of the multiscale method discussed here is a necessary condition for a consistent operator, and follows from the principle of linear superposition. The sum of the basis function solutions is unity at any point in the domain, thus the sum of basis function fluxes at any interface is zero by linear superposition and therefore from Eq. 4.4 the sum of the fine scale flux coefficients is zero when $\phi_{H_j} = 1$ for all j, so that

$$\Sigma_{j=1}^{N_f} t_{i,j}^* = 0 \tag{4.6}$$

As discussed below, the coarse operator is constructed from a linear combination of the fine scale operator coefficients and consistency of the coarse operator follows from consistency of the fine scale operator. Both embedded Dirichlet and Neumann-D basis functions have proven to be quite effective, a basis function solution is illustrated in Fig. 7b.

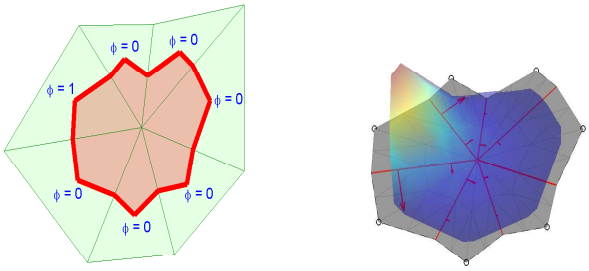

(a) (b)

FIG. 7. *(a) Boundary conditions for Neumann-D basis functions (dirichlet pressure set at associated fine grid corner cell centre, thick red line indicates no flow boundary) (b) Example basis function solution*

The results obtained from using embedded Dirichlet and Neumann-D basis functions are presented and compared in a number of examples in the results section sec.5.

Neumann-D and embedded Dirichlet basis functions lead to two unstructured grid MSFV formulations. The consistency condition is always satisfied by both formulations and grid complexity does not appear to affect the solution in most cases. Embedded Dirichlet basis functions provide a natural extension of the original basis functions to distorted quadrilateral and triangular unstructured grids. The boundary conditions of the Neumann-D basis functions offer a natural flow based boundary condition which force zero flux around each dual-cell perimeter uniformly. The same imposed zero flux is seen by each dual, while for the Dirichlet basis functions neighbouring dual cells see discontinuous fluxes. In that sense the Neumann-D formulation may be viewed as a natural counterpart to what happens in the multiscale method at the reconstruction stage, where flux is continuous between neighbouring coarse cell boundaries and pressure is discontinuous.

4.4. Coarse Scale Operator. The Neumann-D and embedded Dirichlet coarse grid operators have been compared on a number of problems by solving equation Eq. 4.2 for well known test cases with a known solution; linear flow, piecewise linear flow, quadratic flow, piecewise quadratic flow on Delaunay and other grid types. The Neumann-D and embedded Dirichlet coarse operator results are both comparable with TPS applied directly to the coarse grid in each case. The coarse operator is assembled from the above local fine scale transmissibility matrices. Each component of the vector of fine flux values of Eq.4.5 from the respective fine scale basis function solutions, are summed to give a total coarse flux per coarse sub-interface with coarse operator transmissibility coefficients resulting in

$$\begin{bmatrix} f_1 \\ f_2 \\ \vdots \\ f_n \end{bmatrix} = \begin{bmatrix} t_{1,1} & t_{1,2} & \cdots & t_{1,n} \\ t_{2,1} & t_{2,2} & \cdots & t_{2,n} \\ \vdots & \vdots & \ddots & \vdots \\ t_{n,1} & t_{n,2} & \cdots & t_{n,n} \end{bmatrix} \begin{bmatrix} \phi_{H_1} \\ \phi_{H_2} \\ \vdots \\ \phi_{H_n} \end{bmatrix} \tag{4.7}$$

where $f_i = \sum f_i^*$ are the coarse interface fluxes and $t_{i,j} = \sum t_{i,j}^*$ where summation is over the respective column vectors. As a result, the coarse grid operators satisfy the necessary consistency condition, together with a zero row sum matrix on general unstructured grids comprised of triangles and/or quadrilaterals.

The fluxes of Eq.4.7 are assembled into the global coarse grid operator matrix. The pressure equation is next solved over the global reservoir on the coarse grid using the locally conservative coarse grid operator, subject to the actual reservoir problem boundary conditions.

4.5. Fine Scale Flux and Pressure Reconstruction. After solving for the coarse grid pressure field ϕ_H over the global reservoir via the coarse grid operator, the resulting coarse grid solution is used to define projected specified flux boundary conditions on to locally refined coarse cell boundaries via

$$\begin{bmatrix} f_1^* \\ f_2^* \\ \vdots \\ f_n^* \end{bmatrix} = \begin{bmatrix} t_{1,1}^* & t_{1,2}^* & \cdots & t_{1,n}^* \\ t_{2,1}^* & t_{2,2}^* & \cdots & t_{2,n}^* \\ \vdots & \vdots & \ddots & \vdots \\ t_{n,1}^* & t_{n,2}^* & \cdots & t_{n,n}^* \end{bmatrix} \begin{bmatrix} \phi_{H_1} \\ \phi_{H_2} \\ \vdots \\ \phi_{H_n} \end{bmatrix} \tag{4.8}$$

where the fine scale transmissibility matrix operates on the known coarse solution vector c.f. Eq.4.8. The locally conservative fine scale solution is then reconstructed by solving Eq. 4.1 over each refined coarse grid cell using the CVD-MPFA method, subject to Neumann conditions defined by Eq.4.8 together with pressure specified at the centre of each coarse cell, also using the coarse grid solution.

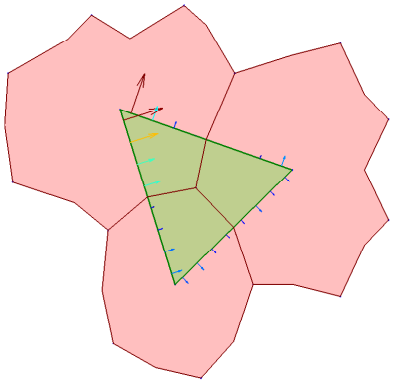

FIG. 8. *Example boundary fluxes derived from basis functions from the encapsulating dual cells*

5. Computational Examples. Several test cases are now presented on grids with increasing complexity in order to show the performance of the Neumann-D and embedded Dirichlet basis functions. Pressure field solutions are displayed as isosurfaces. We also show streamlines and tracer concentration fields for cases 3 and 4, involving heterogeneous SPE10 data. Note that the concentration field is updated via a first order upwind finite-volume method, which with the exception of fluxes on refined coarse cell boundaries, involves an otherwise standard explicit update. The

fine cell-face tracer concentration on a refined coarse cell boundary, is defined by upwinding, with cell-face concentration set equal to the left or right adjacent fine cell concentration value, according to the sign of the projected conservative flux on the common boundary c.f. Eq. 4.8. The resulting locally conservative fine cell-face tracer flux is then defined by the product of cell-face concentration multiplying the projected conservative flux on the boundary.

In all of the multiscale results presented pressure remains discontinuous on coarse cell boundaries. This is to be expected and is consistent with the original multiscale methodology, where only flux continuity is enforced on coarse cell boundaries and no iteration is employed as is the case here.

Comparisons of the respective multiscale methods using embedded Dirichlet and Neumann-D basis functions on a Cartesian grid show that multiscale with either of the generalised basis functions described here are able to reproduce the resolution of the original MSFV.
For all other grid types considered multiscale with Neumann-D and embedded Dirichlet basis functions consistently yield relatively well resolved solutions.

In this section we shall now refer to multiscale with embedded Dirichlet basis functions by MSFVd, and multiscale with Neumann-D basis functions as MSFVn.

The grids used range from simple Cartesian grids Fig.9a, quadrilateral grids Fig.9b, equilateral grids Fig.9c and fully unstructured triangular grids Fig.9d. These grids are used to help show a transition from the basic Cartesian grid to generic unstructured triangle grids.

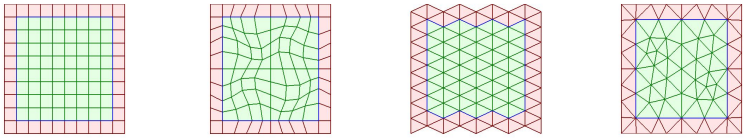

(a) (b) (c) (d)

FIG. 9. *Coarse grids used: (a) Cartesian (b) Distorted Cartesian (c) Equilateral (d) Unstructured tri. Green and red cells represent domain and ghost cells respectively to distinguish between cells that are used in boundary pressure specification and those being solved for.*

When internal boundaries are present the structured and unstructured grids are boundary aligned.
The reconstructed fine scale solutions computed using MSFVd and MSFVn are shown for each test case. The coarse grids used for each test case are shown in Fig. 9.

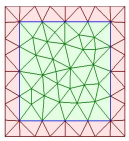

FIG. 10. *Delaunay grid used for heterogeneous examples*

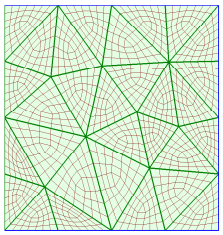

FIG. 11. *Example fine grid from refined coarse cells*

Case 1. This example involves a discontinuous diagonal isotropic tensor field with permeability jump in magnitude from 100 to 1 half way across the domain with a piecewise linear exact solution. The reference solution shown in Fig. 12a highlights the effect of permeability discontinuity in the field, aligned horizontally across the centre of the domain. The permeability tensor above and below the discontinuity is $\begin{bmatrix} 100 & 0 \\ 0 & 100 \end{bmatrix}$ and $\begin{bmatrix} 1 & 0 \\ 0 & 1 \end{bmatrix}$ respectively. The exact solution is used to define Dirichlet boundary conditions for the test problem. The reconstructed fine scale solutions, computed on a Cartesian grid, resulting from multiscale with embedded Dirichlet and Neumann-D basis functions respectively are shown for reference, Fig. 12b,12c. For all other grid types both MSFVn, Figs.(13,14,15)a and MSFVd, Figs.(13,14,15)b, results are good approximations of the finescale reference solution. We point out here that results, particularly on equilateral triangle grids may appear inaccurate or distorted, MSFVn has some oscillations on boundaries, while MSFVd has less oscillation on boundaries, in particular Fig. 14, though the effect of the particular viewing angle being used in combination with the resulting jagged boundary edge of the grid also has an effect.

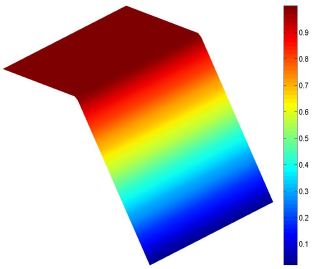

(a)

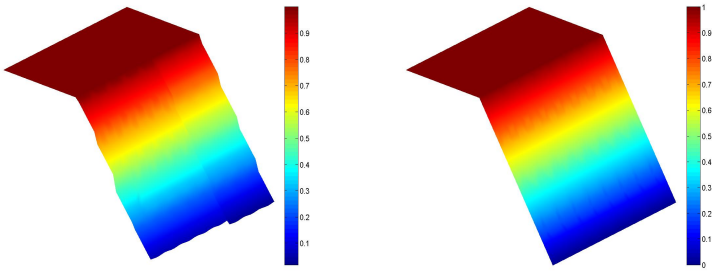

(b) (c)

FIG. 12. *Case 1, (a) Reference solution, Fine scale Cartesian grid Fig.9a reconstruction : (b) MSFVn (c) MSFVd*

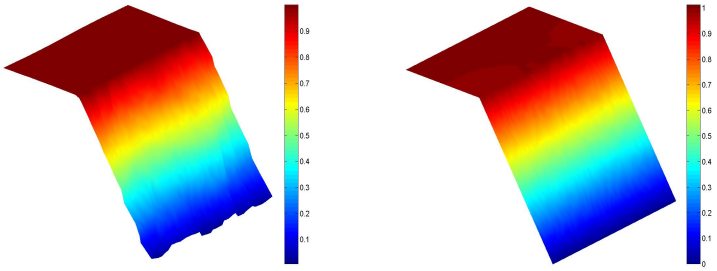

(a) (b)

FIG. 13. *Case 1, quadrilateral grid Fig.9b, Reconstructed pressure fields : (a) MSFVn (b) MSFVd*

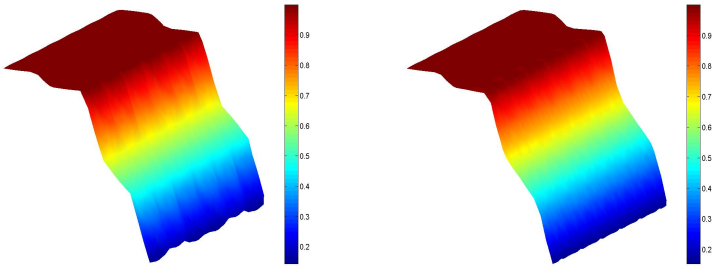

(a) (b)

FIG. 14. *Case 1, equilateral triangle grid Fig.9c, Reconstructed pressure fields : (a) MSFVn (b) MSFVd*

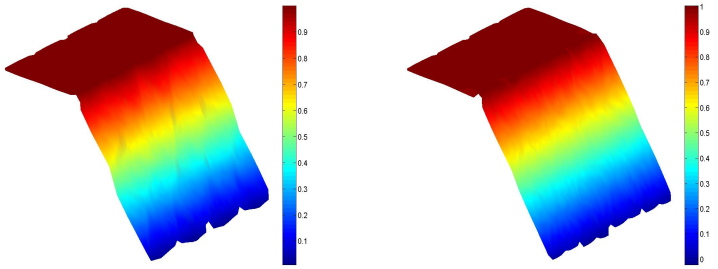

(a) (b)

FIG. 15. *Case 1, unstructured triangle grid Fig.9d, Reconstructed pressure fields : (a) MSFVn (b) MSFVd*

Case 2. This problem has a piecewise quadratic solution [9] where the discontinuity is aligned vertically along the centre of the domain. Here the permeability tensor to the left and right of the discontinuity is $\begin{bmatrix} 50 & 0 \\ 0 & 1 \end{bmatrix}$ and $\begin{bmatrix} 1 & 0 \\ 0 & 10 \end{bmatrix}$ respectively. This example involves a discontinuous anisotropic tensor with variable grid geometry leading to stronger full-tensor effects. The exact solution is used to define Dirichlet boundary conditions for the test problem. The reference solution is shown in Fig. 16a, with the respective reconstructed fine scale solutions for each basis function type computed on a Cartesian grid, shown in Fig.16b and 16c indicating comparable performance. We note that as before, particularly on equilateral triangle grids that MSFVn has some oscillations on boundaries, while MSFVd has less oscillation on boundaries Fig. 19. Though generally on irregular grids both the MSFVn, Figs.(17,19,20)a and MSFVd, Figs.(17,19,20)b, solutions give good approximations of the finescale reference. Finally we note the result of using a two-point flux approximation (TPFA) in MSFV on a non K-orthogonal quadrilateral grid in Fig. 18(d) and planar view in 18(f), compared to the exact solution in Fig. 18(a) and planar view in Fig. 18(b). As expected the method yields a solution with inherent grid orientation due to the well known inconsistency of the approximation on such grids e.g. [9]. The results from the consistent CVD-MPFA method are shown along side in Fig. 18(c,e) and motivate the

need for the development of MSFV based on the CVD-MPFA formulation, presented here.

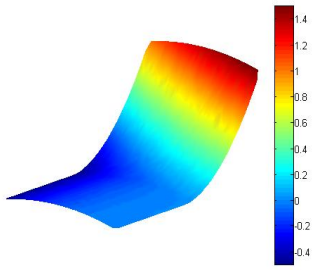

(a)

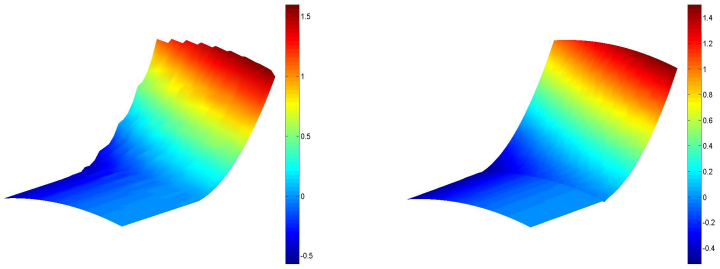

(b) (c)

FIG. 16. *Case 2: (a) Reference solution, Fine scale Cartesian grid Fig.9a. Reconstruction : (b) MSFVn (c) MSFVd*

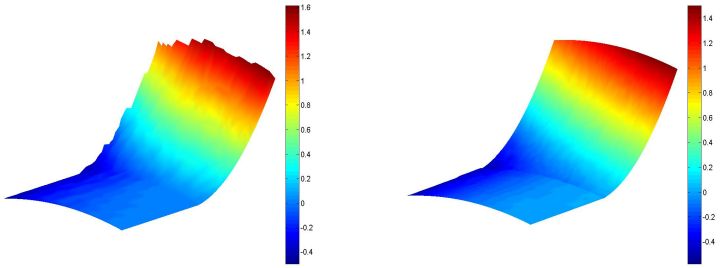

(a) (b)

FIG. 17. *Case 2, quadrilateral grid Fig.9b, Reconstructed pressure fields : (a) MSFVn (b) MSFVd*

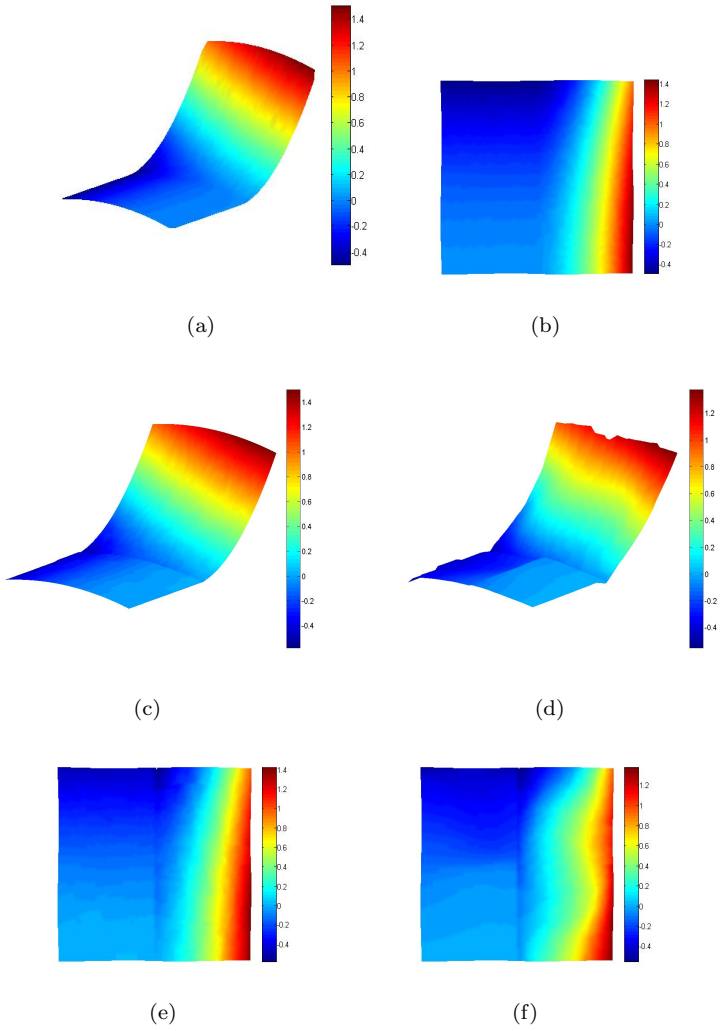

FIG. 18. *Case 2, quadrilateral grid Fig.9d, (a) Exact solution (b) Planar view: exact solution. Reconstructed pressure fields : (c) MSFVd using CVD-MPFA (d) MSFVd using TPFA (e) Planar view: MSFVd using CVD-MPFA (f) Planar view: MSFVd using TPFA*

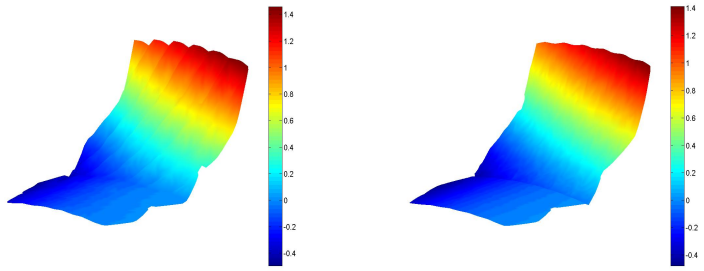

(a) (b)

FIG. 19. *Case 2, equilateral triangle grid Fig.9c, Reconstructed pressure fields : (a) MSFVn (b) MSFVd*

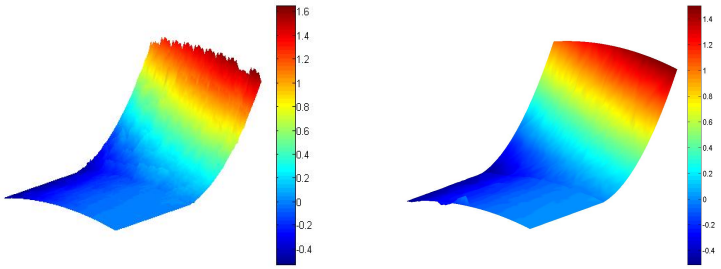

(a) (b)

FIG. 20. *Case 2, unstructured triangle grid Fig.9d, Reconstructed pressure fields : (a) MSFVn (b) MSFVd*

Case 3. This case involves a heterogeneous permeability field taken from SPE10 data commonly used as a benchmark for pressure/transport solvers. The permeability data is taken from the Tarbert layers section. For each grid type the Cartesian index system used in the SPE10 data set is projected onto the fine scale grid by locating nearest points Fig.21a. This can lead to very slight variations in the permeability field between grid types but still serves as a good comparison of each grid type. Boundary conditions involve specification of high pressure on the left hand boundary and low pressure on the right hand boundary of the rectangular domain, together with zero normal flux conditions specified on the top and bottom walls respectively. The tracer concentration is initially zero in the field and specified to be unity on the left hand boundary. The fine scale reference solution is shown in Fig. 22b. The reconstructed fine scale solution for both basis function types is shown in Fig.22c and 22d on Cartesian grids, where both methods yield physically meaningful solutions. Both the streamline, Fig.(23 and tracer plots Fig.24, demonstrate good agreement between the multiscale results and the finescale reference solution. The solutions for other gridtypes: quadrilateral grid Fig's.25,26,27, equilateral triangle grid Fig's.28,29,30 and Delaunay grid Fig's.31,32,33, show that the generalised MSFVd and MSFVn multiscale methods also yield good comparative performance for the example SPE10 data. On close inspection there are only minor differences in small areas

between the MSFVn and MSFVd results.

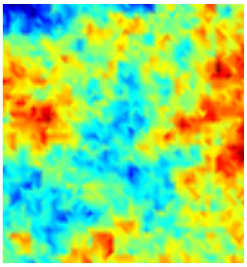

FIG. 21. *Case 3: Logarithmic x Permeability field within the Tarbert layer*

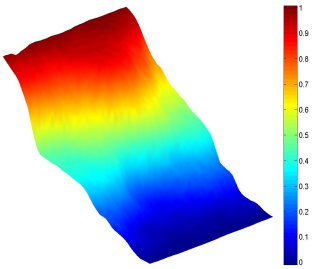

(a)

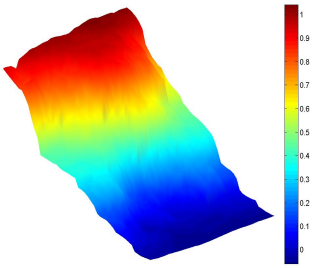

(b)

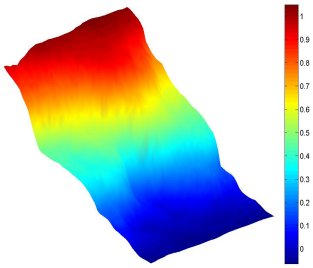

(c)

FIG. 22. *Case 3, Cartesian grid Fig.9a, (a) Reference solution, Finescale reconstruction : (b) MSFVn (c) MSFVd*

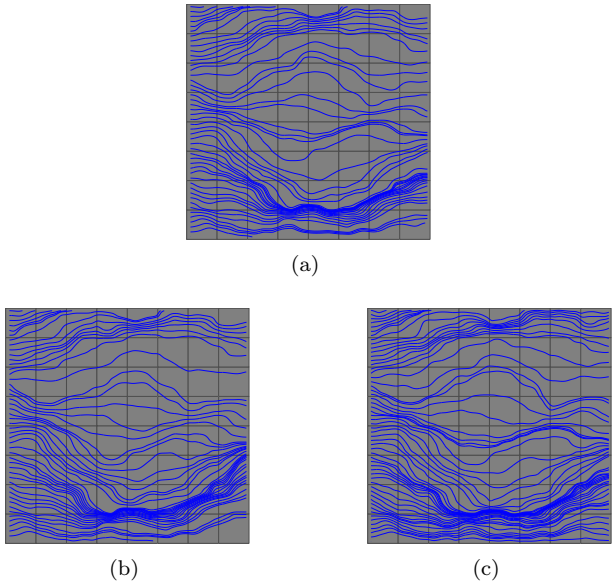

FIG. 23. *Case 3, Cartesian grid, Finescale streamline plot (Coarse grid shown) (a) Reference (b) MSFVn (c) MSFVd*

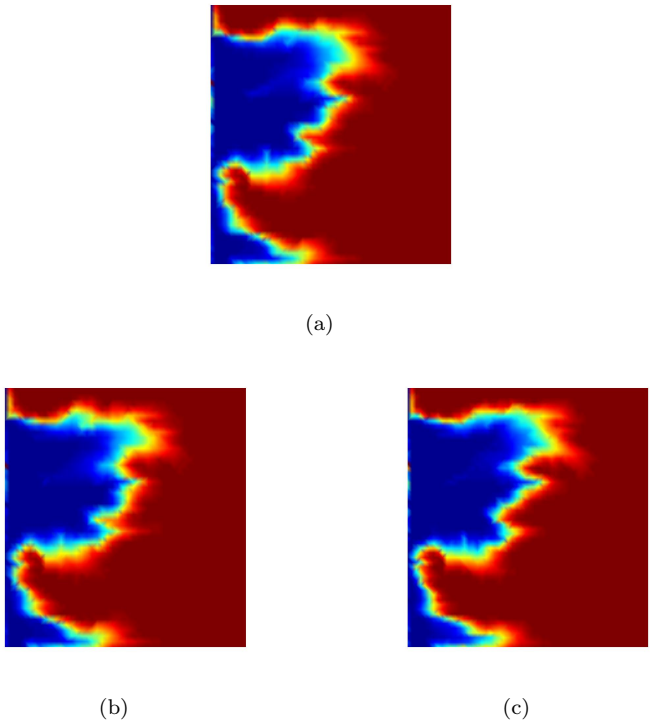

FIG. 24. *Case 3, Cartesian grid, Tracer plot at 0.3 PVI (a) Reference (b) MSFVn (c) MSFVd*

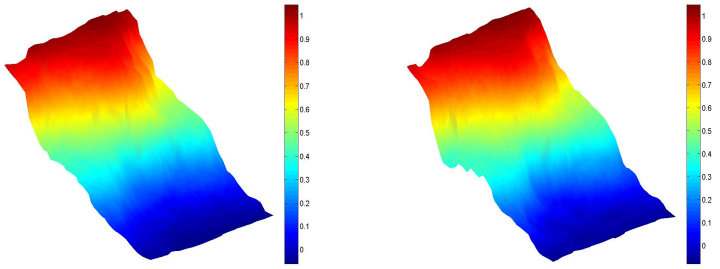

(a) (b)

FIG. 25. *Case 3, quadrilateral grid Fig.9b, Reconstructed pressure fields : (a) MSFVn (b) MSFVd*

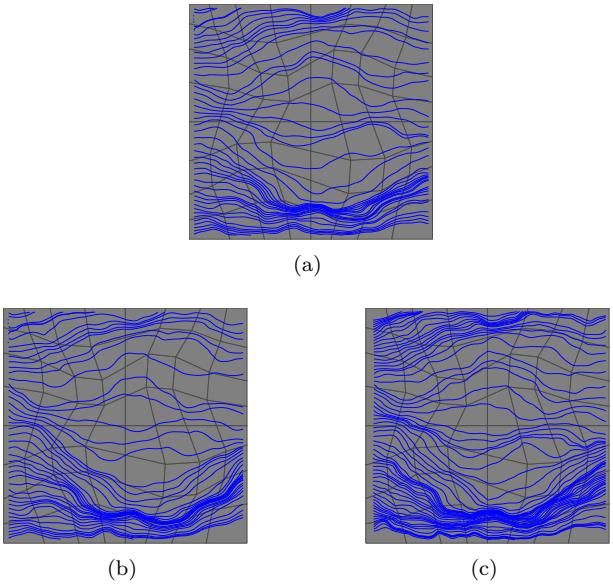

(a)

(b) (c)

FIG. 26. *Case 3, quadrilateral grid, Finescale streamline plot (Coarse grid shown) (a) Reference (b) MSFVn (c) MSFVd*

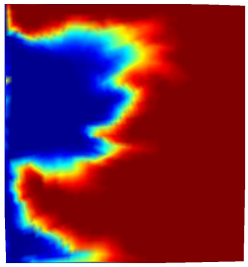

(a)

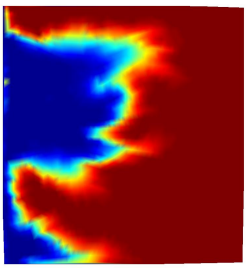

(b)

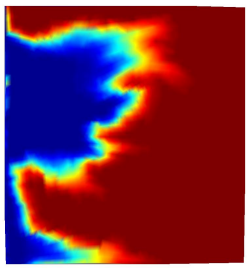

(c)

FIG. 27. *Case 3, quadrilateral grid, Tracer plot at 0.3 PVI (a) Reference (b) MSFVn (c) MSFVd*

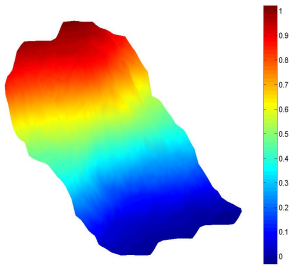

(a)

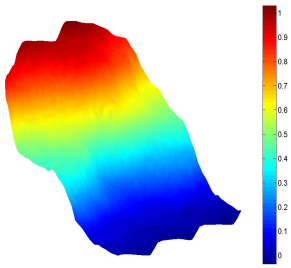

(b)

FIG. 28. *Case 3, equilateral triangle grid Fig.9c, Reconstructed pressure fields : (a) MSFVn (b) MSFVd*

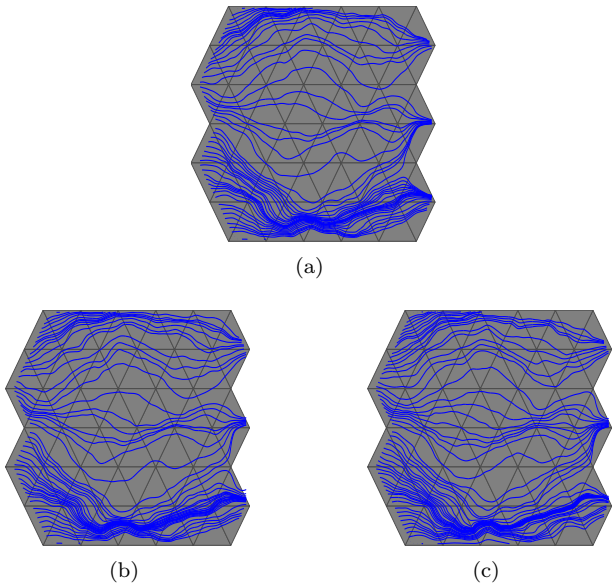

FIG. 29. *Case 3, equilateral triangle grid, Finescale streamline plot (Coarse grid shown) (a) Reference (b) MSFVn (c) MSFVd*

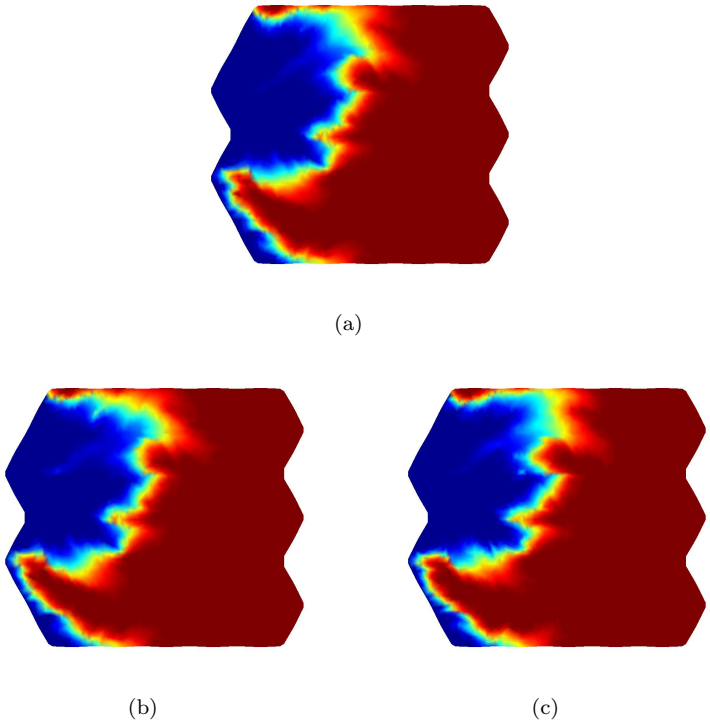

FIG. 30. *Case 3, equilateral triangle grid, Tracer plot at 0.3 PVI (a) Reference (b) MSFVn (c) MSFVd*

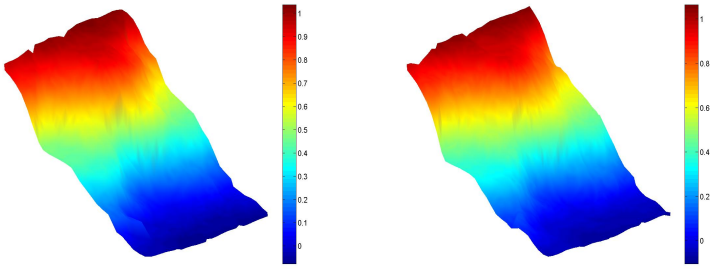

(a) (b)

FIG. 31. *Case 3, Unstructured triangle grid Fig.9d, Reconstructed pressure fields : (a) MSFVn (b) MSFVd*

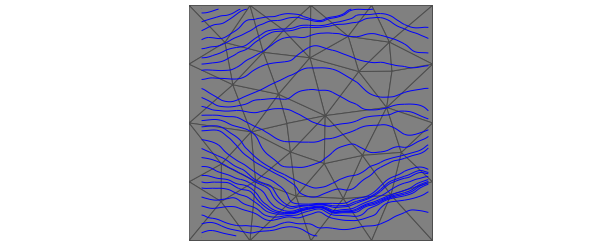

(a)

(b) (c)

FIG. 32. *Case 3, Unstructured triangle grid, Finescale streamline plot (Coarse grid shown) (a) Reference (b) MSFVn (c) MSFVd*

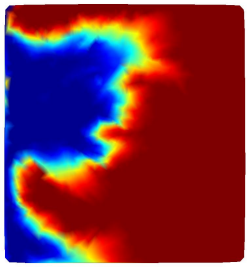

(a)

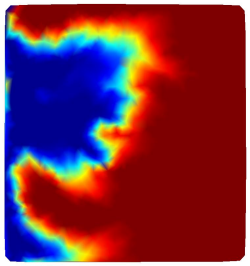

(b)

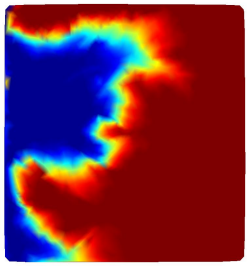

(c)

FIG. 33. *Case 3, Unstructured triangle grid, Tracer plot at 0.3 PVI (a) Reference (b) MSFVn (c) MSFVd*

Case 4. A second case using data from the SPE10 permeability field, this time from the more challenging Upper Ness layers is presented. This example was chosen to challenge the methods in the presence of strong heterogeneity Fig.34a. Boundary conditions again involve specification of high pressure on the left hand boundary and low pressure on the right hand boundary of the rectangular domain, together with zero normal flux conditions specified on the top and bottom walls respectively. The tracer concentration is initially zero in the field and specified to be unity on the left hand boundary. This case then follows the same format as case 3. The solutions for the four gridtypes are given in: cartesian grid Fig's.35, 36,37; quadrilateral grid Fig's. 38,39,40; equilateral triangle grid Fig's. 41,42,43 and Delaunay grid Fig's. 44,45,46. We note that the MSFVd method (using embedded Dirichlet basis functions) exhibit very large spurious oscillations in the reconstructed pressure field in Fig's.35, 38, 44. In contrast the MSFVn method (using Neumann-D basis functions) copes with the strong heterogeneity. Although there are some differences in the respective MSFVn tracer plots when compared to the finescale reference solution, the larger part of the respective MSFVn solutions share the character of the reference solution. However, we also note that the MSFVd pressure field oscillations are located at coarse cell boundaries. In contrast oscillations are not seen in the corresponding MSFVd streamline and tracer plots, which is attributed to the use of the specified flux condition on the coarse cell boundaries. The respective MSFVd tracer solutions Fig's. 37c, 40c, 43c, 46c, are seen to capture the features of the reference grid tracer solution shown in Fig's. 37a, 40a, 43a, 46a.

The MSFVd and MSFVn schemes are compared in terms of condition number ratios ($MSFVd/MSFVn$) below for the SPE10 Upper Ness test case.

	Basis Function	Coarse Operator
Cartesian Grids	1.16	1.03
Distorted Quadrilateral Grids	0.076	1.682
Equilateral Triangle Grids	0.810	0.671
Delaunay Grids	0.921	0.641

TABLE 1

SPE10 Upper Ness. Condition number ratios (MSFVd/MSFVn): Fine-scale Operator of Basis Function, and the Coarse Operator for each grid type

The ratios show that similar condition numbers are obtained by the two types of basis function both in terms of average number for the basis functions, and for the respective coarse grid operators, except for the quadrilateral grid. The most notable difference is for the quadrilateral grid, where the Neumann-D basis function operator has an order of magnitude larger condition number than the Dirichlet operator, although the coarse grid Dirichlet operator condition number is slightly larger than the respective Neumann-D operator.

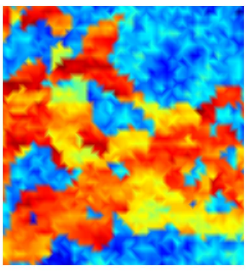

FIG. 34. *Case 4: Logarithmic x Permeability field within the Upper Ness layer*

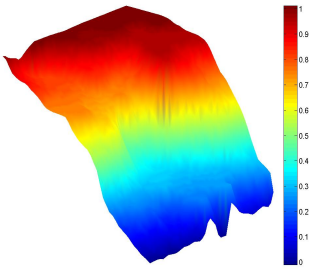

(a)

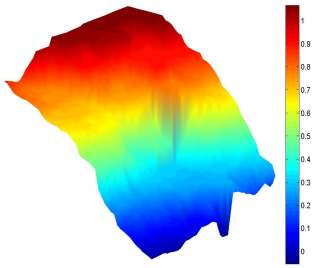

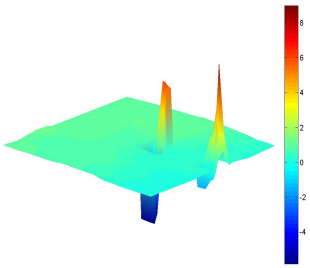

(b) (c)

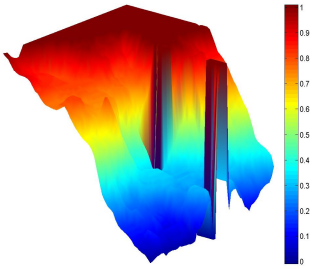

(d)

FIG. 35. *Case 4, Fine scale Cartesian grid Fig.9a, (a) Reference solution, finescale reconstruction : (b) MSFVn (c) MSFVd (d) MSFVd with Capped errors*

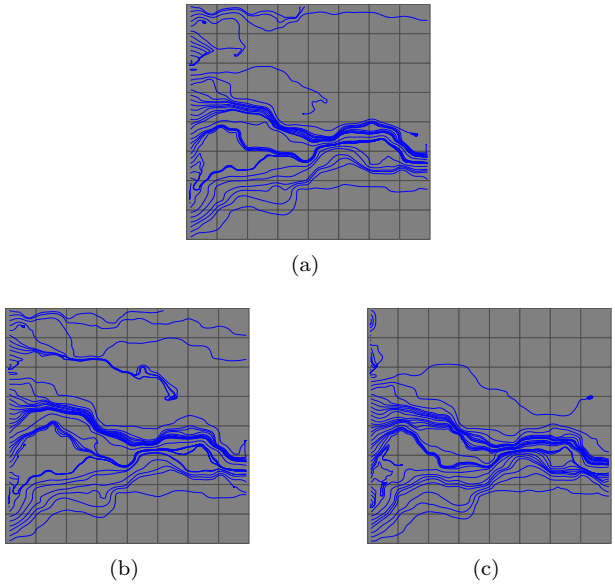

(a)

(b) (c)

FIG. 36. *Case 4, Fine scale Cartesian grid, Finescale streamline plot (Coarse grid shown) (a) Reference (b) MSFVn (c) MSFVd*

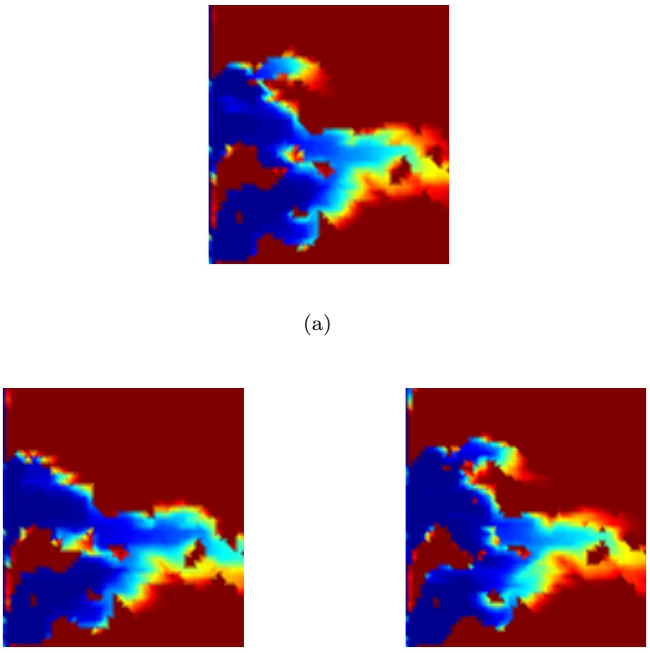

(a)

(b) (c)

FIG. 37. *Case 4, Fine scale Cartesian grid, Tracer plot at 0.3 PVI (a) Reference (b) MSFVn (c) MSFVd*

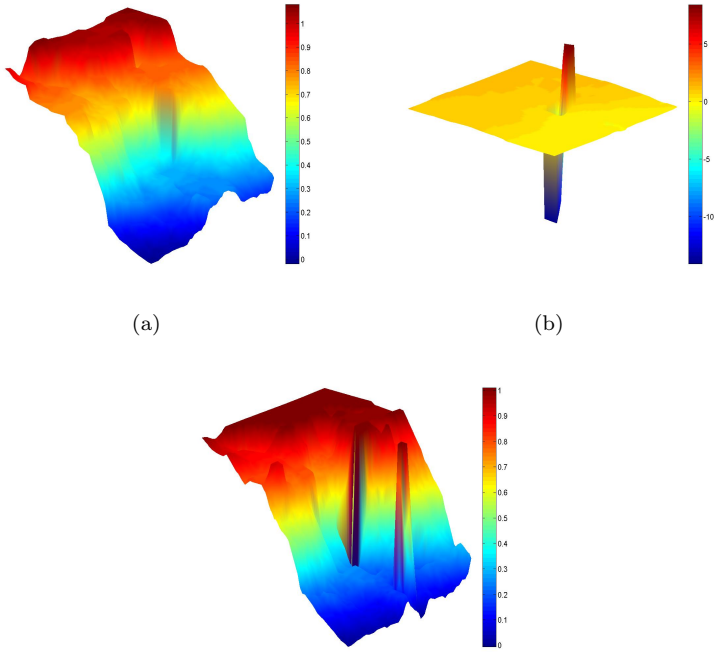

(a) (b)

(c)

FIG. 38. *Case 4, quadrilateral grid Fig.9b, Reconstructed pressure fields : (a) MSFVn (b) MSFVd (c) MSFVd with Capped errors*

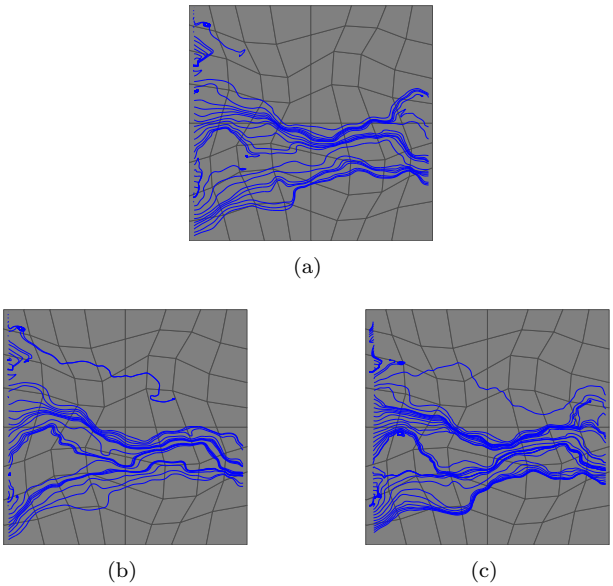

(a)

(b) (c)

FIG. 39. *Case 4, quadrilateral grid, Finescale streamline plot (Coarse grid shown) (a) Reference (b) MSFVn (c) MSFVd*

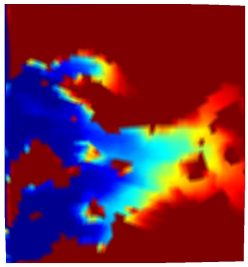

(a)

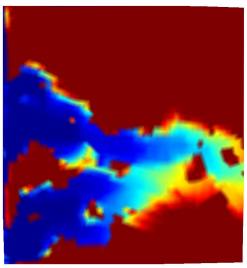

(b)

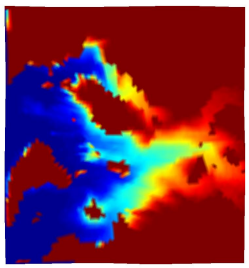

(c)

FIG. 40. *Case 4, quadrilateral grid, Tracer plot at 0.3 PVI (a) Reference (b) MSFVn (c) MSFVd*

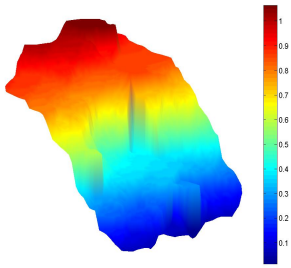

(a)

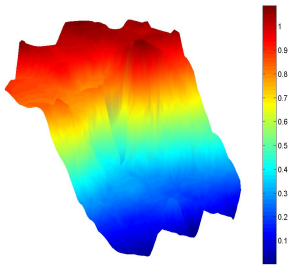

(b)

FIG. 41. *Case 4, equilateral triangle grid Fig.9c, Reconstructed pressure fields : (a) MSFVn (b) MSFVd*

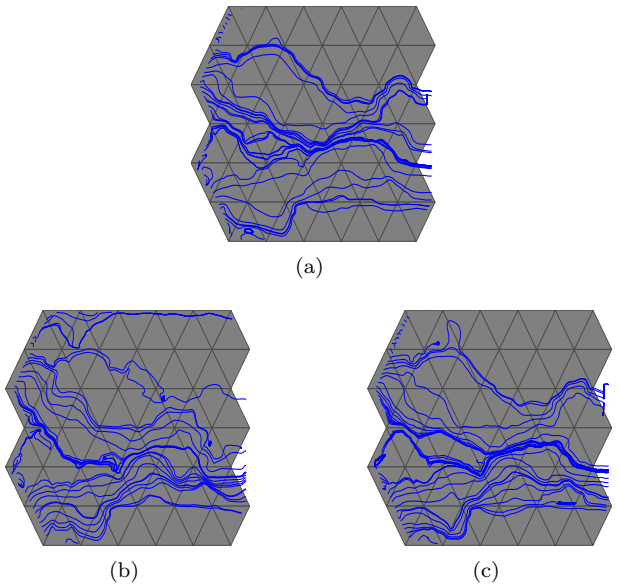

FIG. 42. *Case 4, equilateral triangle grid, Finescale streamline plot (Coarse grid shown) (a) Reference (b) MSFVn (c) MSFVd*

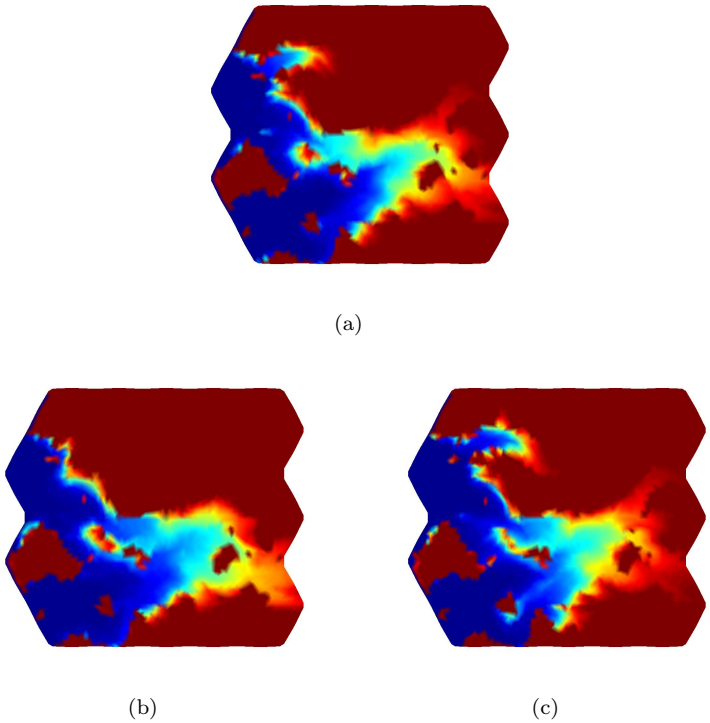

FIG. 43. *Case 4, equilateral triangle grid, Tracer plot at 0.3 PVI (a) Reference (b) MSFVn (c) MSFVd*

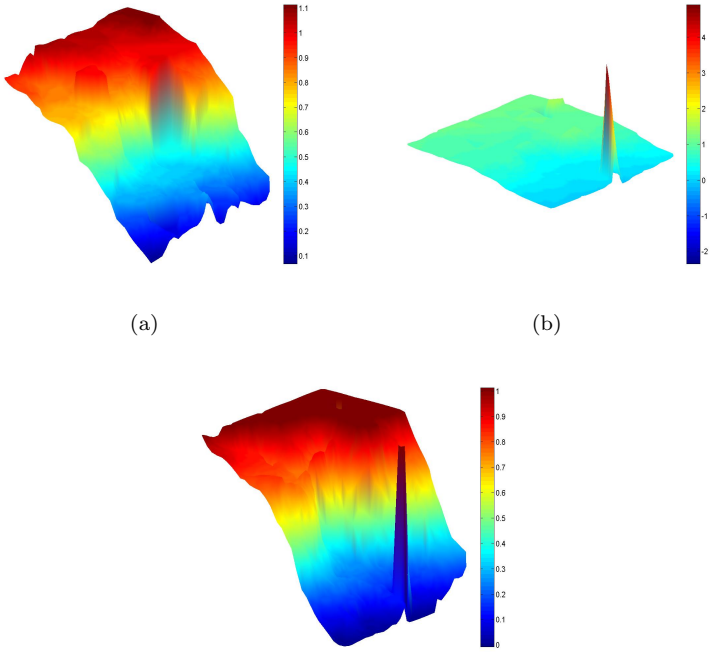

(a) (b)

(c)

FIG. 44. *Case 4, Unstructured triangle grid Fig.9d, Reconstructed pressure fields : (a) MSFVn (b) MSFVd (c) MSFVd with Capped errors*

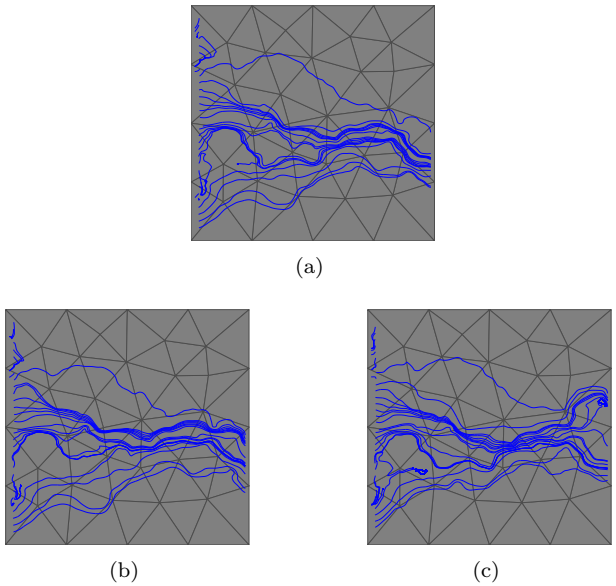

(a)

(b) (c)

FIG. 45. *Case 4, Unstructured triangle grid, Finescale streamline plot (Coarse grid shown) (a) Reference (b) MSFVn (c) MSFVd*

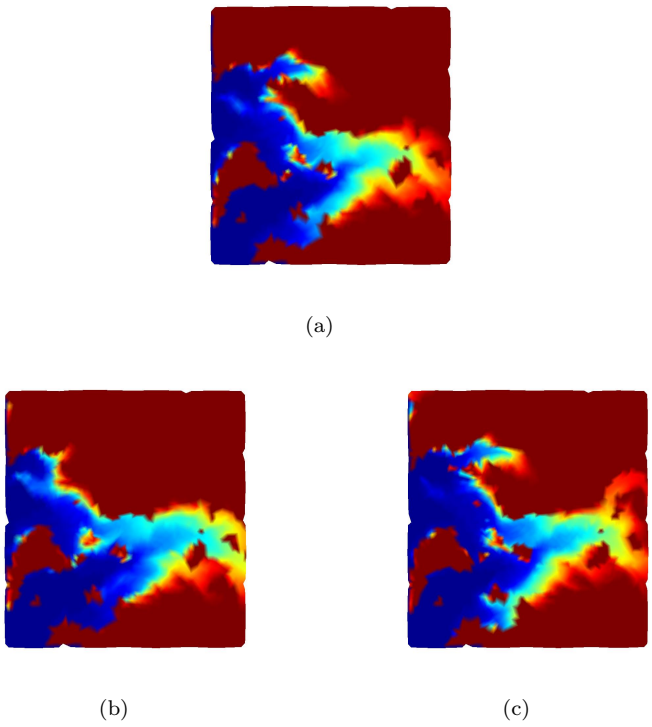

(a)

(b) (c)

FIG. 46. *Case 4, Unstructured triangle grid, Tracer plot at 0.3 PVI (a) Reference (b) MSFVn (c) MSFVd*

6. Conclusions. Novel multiscale finite volume methods are presented for quadrilateral and triangular unstructured grids in two spatial dimensions using a CVD-MPFA formulation. A comparison between MSFV with a two-point flux approximation versus MSFV with CVD-MPFA on a non K-orthogonal grid motivates the need for a CVD-MPFA based MSFV formulation.

The currently established multiscale Dirichlet basis functions are generalised for MSFV on quadrilateral and triangular unstructured grids using the CVD-MPFA formulation. The generalisation of Dirichlet basis functions to quadrilateral and triangular unstructured grids involves generating fine grids over coarse dual-cells, with the coarse dual-cell boundaries being embedded in the fine grid perimeter cells, leading to natural imposition of embedded Dirichlet boundary conditions.

Neumann-D basis functions are also proposed which lead to a novel multiscale variant. Both the embedded Dirichlet basis functions and the Neumann-D basis functions yield (necessary) consistent transmissibility coefficients.

Several test cases are presented including anisotropic permeability tensors and heterogeneous permeability fields. In all cases except the SPE10 upper Ness layer, the embedded Dirichlet and Neumann-D based multiscale methods are both able to yield results of resolution that is comparable with the original Cartesian grid multiscale method, with similar resolution obtained on quadrilateral and triangular structured and unstructured grids. For the SPE10 upper Ness layer test case, the embedded Dirichlet based multiscale method captures more of the flow field features. While

some flow field discrepencies are observed between the respective Neumann-D and embedded Dirichlet based multiscale method flow field results, the Neumann-D based multiscale method yields pressure fields that do not suffer from the excessive oscillations that occur with the Dirichlet based method on both structured and unstructured grids.

Acknowledgements. We thank the referees for their constructive comments. EPSRC financial support is acknowledged.

REFERENCES

[1] J. M. Nordbotten A. Sandvin and I. Aavatsmark, *Multiscale mass conservative domain decomposition preconditioners for elliptic problems on irregular grids*, Computational Geosciences, 15 (2011), pp. 587–602.

[2] I. Aavatsmark, T. Barkve, Ø. Bøe, and T. Mannseth, *Discretization on unstructured grids for inhomogenous, anisotropic media. Part I: Derivation of the methods*, SIAM Journal on Scientific Computing, 19 (1998), pp. 1700–1716.

[3] T. Arbogast, G. Pencheva, M. F. Wheeler, and I. Yotov, *A multiscale morter mixed finite element method*, SIAM Multiscale Model Sim, 6 (2007), pp. 319–346.

[4] F. Brezzi and M. Fortin, *Mixed and Hybrid Finite Elements Methods*, Springer Series in Computational Mathematics 15, Springer-Verlag, 1991.

[5] D. E. Heath C. L. Farmer and R. O. Moody, *A global optimization approach to grid generation*, 11th SPE Reservoir Simulation Symposium, (1991), pp. 341–350.

[6] Z. Cai, J. E. Jones, S. F. McCormick, and T. F. Russell, *Control-volume mixed finite element methods*, Computational Geosciences, 1 (1997), pp. 289–315.

[7] L. Durlofsky, *A triangle based mixed finite volume technique for modelling two phase flow through porous media*, Journal of Computational Physics, (1993), pp. 252–266.

[8] M. G. Edwards, *Unstructured, control-volume distributed, full-tensor finite-volume schemes with flow based grids*, Computational Geosciences, 6 (2002), pp. 433–452.

[9] M. G. Edwards and C. F. Rogers, *Finite volume discretization with imposed flux continuity for the general tensor pressure equation*, Computational Geosciences, 2 (1998), pp. 259–290.

[10] Y. Efendiev, V. Ginting, T. Hou, and R. Ewing, *Accurate multiscale finite element methods for two phase flowsimulations*, Journal of Computational Physics, 220 (2006), pp. 155–174.

[11] R. Eymard, T. Gallout, and R. Herbin, *A cell centered finite-volume approximation for anisotropic diffusion operators on unstructured meshes in any space dimension*, IMA Journal on Numerical Analysis, 26 (2006), pp. 326–353.

[12] H. A. Friis and M. G. Edwards, *A family of mpfa finite volume schemes with full pressure support for the general tensor pressure equation on cell-centered triangular grids*, Journal of Computational Physics, 230 (2011), pp. 205–231.

[13] H. A. Friis, M. G. Edwards, and J. Mykkeltveit, *Symmetric positive definite flux-continuous full-tensor finite-volume schemes on unstructured cell centered triangular grids.*, SIAM Journal on Scientific Computing, 31 (2008), pp. 1192–1220.

[14] D. Karvounis H. Hajibeygi and P. Jenny, *A hierarchical fracture model for the iterative multiscale finite volume method*, Journal of Computational Physics, 230 (2011), p. 87298743.

[15] F. Hermeline, *A finite volume method for the approximation of diffusion operators on distorted meshes*, Journal of Computational Physics, 160 (2000), pp. 481–499.

[16] M. Hesse, B.T. Mallinson, and H A. Tchelepi, *Compact multiscale finite volume method for heterogeneous anisotropic elliptic equations*, SIAM Multiscale Model Sim, 7 (2008), pp. 934–962.

[17] T. Y. Hou and X. H. Wu, *A multiscale finite element method for elliptic problems in composite materials and porous media*, Journal of Computational Physics, 134 (1997), pp. 169–189.

[18] J. Hyman, M. Shashkov, and S. Steinberg, *The numerical solution of diffusion problems in strongly heterogeneous non-isotropic materials*, Journal of Computational Physics, 132 (1997), pp. 130–148.

[19] S. Krogstad J. E. Aarnes and K. A. Lie, *Multiscale mixed/mimetic methods on corner-point grids*, Computational Geosciences, 12 (2008), pp. 297–315.

[20] P. Jenny, S. H. Lee, and H. A. Tchelepi, *Multiscale finite-volume method for elliptic problems in subsurface flow simulation*, Journal of Computational Physics, 187 (2003), pp. 47–67.

[21] ———, *Adaptive multiscale finite volume method for multiphase flow and transport*, SIAM Multiscale Model Sim, 3 (2004), pp. 50–64.

[22] V. Kippe, J. E. Aarnes, and K. A. Lie, *A comparison of multiscale methods for elliptic methods in porous media flow*, Computational Geosciences Special Volume on Multiscale Methods, 12 (2008), pp. 377–398.

[23] C. Le Potier, *Finite volume scheme for highly anisotropic diffusion operators on unstructured meshes*, C. R., Math., Acad. Sci. Paris, Ser. I, 340 (2005), pp. 921–926.

[24] S. H. Lee, L. J. Durlovsky, M. F. Lough, and W. H. Chen, *Finite difference simulation of geologically complex reservoirs with tensor permeabilities*, SPE Reservoir Evaluation & Engineering, 1 (1998), pp. 567–574.

[25] K. Lipnikov, M. Shashkov, and D. Svyatskiy, *The mimetic finite difference discretization of diffusion problem on unstructured polyhedral meshes*, Journal of Computational Physics, 211 (2006), pp. 473–491.

[26] O. Moyner and K. A. Lie, *The multiscale finite-volume method on stratigraphic grids*, Society of Petroleum Engineers Journal, 19 (2013), pp. 816–831.

[27] J. M. Nordbotten and P. Bjorstad, *On the relationship between the multiscale finite-volume method and domain decomposition preconditioners*, Computational Geosciences, 12 (2013), pp. 367–376.

[28] E. Parramore, M.G.Edwards, M. Pal, and S. Lamine, *Cvd-mpfa based multiscale formulation on structured and unstructured grids*, in ECMOR XIII - 13th European Conference on the Mathematics of Oil Recovery, Biarritz, France 10-13th Sept, 2012.

[29] ———, *Multiscale formulations with cvd-mpfa schemes on structured and unstructured grids*, in SPE Reservoir Simulation Symposium, Woodlands, Houston Texas, USA 18th-20th Feb,, 2013.

[30] T. H. Sandve, E. Keilegavlen, and J. M. Nordbotten, *Physics-based preconditioners for flow in fractured porous media*, Water Resources Research, 50 (2014), pp. 1357–1373.

[31] M. Wheeler and I. Yotov, *A multipoint flux mixed finite element method*, SIAM Journal on Numerical Analysis, 44 (2006), pp. 2082–2106.